

Monte Carlo simulations of vector pseudospins for strains: Microstructures, and martensitic conversion times

N. Shankaraiah

School of Physical Sciences, Jawaharlal Nehru University, New Delhi 110067, India.

(Dated: August 26, 2021)

We present systematic temperature-quench Monte Carlo simulations on discrete-strain pseudospin model Hamiltonians to study microstructural evolutions in 2D ferroelastic transitions with two-component vector order parameters ($N_{OP} = 2$). The zero value pseudospin is the single high-temperature phase while the low-temperature phase has N_v variants. Thus the number of nonzero values of pseudospin are triangle-to-centered rectangle ($N_v = 3$), square-to-oblique ($N_v = 4$) and triangle-to-oblique ($N_v = 6$). The model Hamiltonians contain a transition-specific Landau energy term, a domain wall cost or Ginzburg term, and power-law anisotropic interaction potential, induced from a strain compatibility condition. On quenching below a transition temperature, we find behaviour similar to the previously studied square-to-rectangle transition ($N_{OP} = 1, N_v = 2$), showing that the rich behaviour found, is generic. Thus we find for two-component order parameters, that the same Hamiltonian can describe both athermal and isothermal martensite regimes for different material parameters. The athermal/isothermal/austenite parameter regimes and temperature-time-transformation diagrams are understood, as previously, through parametrization of effective-droplet energies. In the athermal regime, we find rapid conversions below a spinodal like temperature and austenite-martensite conversion delays above it, as in the experiment. The delays show early incubation behaviour, and at the transition to austenite the delay times have Vogel-Fulcher divergences and are insensitive to Hamiltonian energy scales, suggesting that entropy barriers are dominant.

PACS numbers: 64.60.De, 81.30.Kf, 64.70.K-, 05.70.Ln

I. INTRODUCTION

Steels and shape memory alloys are martensitic materials that undergo diffusionless, first-order phase transformation from high-temperature parent 'austenite' unit-cell to low-temperature product 'martensite' unit-cells (or variants) on cooling or under external stress¹. A subset of physical strains are the order parameter (OP). As martensitic materials have many applications^{1,2}, much work has been done to understand domain-wall microstructures and their underlying kinetics. According to traditional classification³, martensites are classified as *athermal*, with rapid milli-second austenite-martensite conversions on cooling below a martensite start temperature and no conversions above it; and *isothermal*, which can have slow or delayed conversions in minutes or hours. But, experiments on athermal martensitic materials have found delayed conversions above the martensite start temperature, where only austenite should exist⁴. Computer simulations of martensitic models could give insights into the classification of martensites and the unexpected delayed-conversions in athermal martensites.

Continuous variable nonlinear free energies are minimized in displacement, phase field, and strain using relaxational dynamics, Monte Carlo (MC) and Molecular dynamics simulations⁵⁻⁹ and the obtained microstructures are consistent with experiment¹⁰, but that can need extensive computer time. More economic discrete-strain clock-like model Hamiltonians¹¹ are systematically derived from continuous strain free energies for different ferroelastic transitions in 2- and 3-spatial dimensions (2D & 3D). Power-law anisotropic interaction potentials,

which arise from the no-defect St.Venant compatibility condition^{11,12}, and orient strain domain walls, have their counterparts induced in pseudo spin Hamiltonians. The microstructures generated from these strain-pseudospin models using local mean-field approximation¹³ are in good agreement with the continuous variable models⁵⁻⁷ and experiments¹⁰.

Systematic temperature-quench MC simulations were performed on the simplest scalar-OP, 3-state pseudospin Hamiltonian for square-to-rectangle (SR) transition¹⁴ and showed both rapid conversions below a spinodal-like temperature and incubation-delays above it, as in experiments⁴ on athermal martensitic materials. The conversion-time delays found to have Vogel-Fulcher divergences, which are insensitive to Hamiltonian energy scales and log-normal distributions, suggesting the dominant role of entropy barriers. An athermal/isothermal martensites regime diagram is predicted in material-parameters; crossover temperatures and domain-wall phases in Temperature-Time-Transformation (TTT) diagrams are understood through parametrization of textures by surrogate droplet energies; and role of power-law potentials are shown to be important for textures and incubations¹⁴. The central question is: Are such conversion-delays in the athermal martensite regime, specific to the scalar-OP transition, or are they generic, appearing in vector-OP transitions?

In this paper, we show that the athermal martensite regime conversion-delays in the scalar-OP ($N_{OP} = 1$) SR transition are generic in three vector-OP ($N_{OP} = 2$) ferroelastic transitions: triangle-centered rectangle ($N_v = 3$); square-oblique ($N_v = 4$); triangle-oblique ($N_v = 6$). Under systematic MC temperature quenches,

we find isothermal parameter regime with slow or delayed conversions and athermal parameter regime that has rapid conversions below a temperature and incubation-delays above it, as in experiment⁴ and scalar-OP SR transition¹⁴. The athermal regime conversion-time delays have Vogel-Fulcher divergences, which are insensitive to Hamiltonian energy scales and log-normal distributions. The athermal/isothermal/austenite regime diagrams are obtained in material parameters. The crossover temperatures and domain-wall phases in the TTT diagram are understood through the parametrization of textures. Microstructures obtained in these transitions are in good agreement with continuous-variable simulations⁵⁻⁷ and experiment¹⁰. We finally show the importance of power-law interaction potentials in the incubation behaviour, and microstructures.

The paper is organised as follows. In Section 2, we outline derivations of the vector-OP strain-pseudospin Hamiltonians. In Section 3, we present the athermal/isothermal martensite regimes and crossover in material parameters. In Section 4, we focus on the athermal martensite regime and present conversion-delay kinetics, parametrization of domain-wall phases in TTT diagram by effective droplet energies, and conversion incubation textures. In Section 5, we present kinetics in the absence of the power-law anisotropic interactions that shows delays without incubation, and Section 6 is a summary.

II. STRAIN-PSEUDOSPIN HAMILTONIANS

In this Section, we state for completeness, the vector-OP strain-pseudospin model Hamiltonians¹¹, that were systematically derived from scaled continuous-strain free-energies¹² for triangle-to-centered rectangle (TCR), square-to-oblique (SO) and triangle-to-oblique (TO) ferroelastic structural transitions.

In 2D, structural transitions have $d(d+1)/2 = 3$ or three distinct physical strains, the compressional (e_1), deviatoric (e_2) and shear (e_3) strains. Of these, (e_2, e_3) are OP ($N_{OP} = 2$) and the e_1 is non-OP ($n = 1$) strains. The scaled free energy has a Landau term \bar{F}_L ; a Ginzburg term, quadratic in the OP gradients \bar{F}_G ; and a seemingly innocuous term, quadratic in the non-OP strains \bar{F}_{non} , that turns out to generate crucial power-law anisotropic interactions between the OP strains¹¹. Thus

$$F = E_0[\bar{F}_L + \bar{F}_G + \bar{F}_{non}] \quad (2.1)$$

Here E_0 is an elastic energy per unit cell. The transition specific Landau term \bar{F}_L has $(N_v + 1)$ degenerate energy minima at the first-order transition as shown in Figure 1. The high-temperature austenite minima is allowed at all temperatures as its existence has to be determined dynamically, and N_v minima are the low-temperature martensite variants. The pseudospin derivation results of Ref 11 are restated here, for completeness.

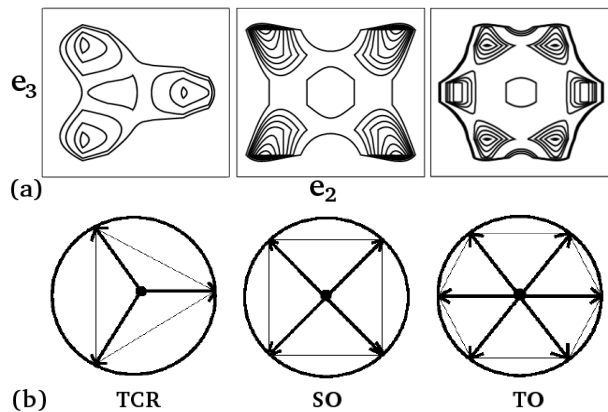


FIG. 1. Landau free energy minima and strain-pseudospin clock vectors: (a) Contours of Landau free energy \bar{F}_L showing single austenite minima at center and N_v martensite minima at corners, in a plot of e_3 versus e_2 and (b) corresponding clock model minima at pseudospin values for TCR (left), SO (middle) and TO (right) transitions.

The scaled Landau free energy \bar{F}_L for TCR transition¹¹

$$\bar{F}_L(\vec{e}) = \sum_{\vec{r}} (\tau - 1) \vec{e}^2 + [\vec{e}^2 - 2(e_2^3 - 3e_2e_3^2) + (\vec{e}^2)^2], \quad (2.2)$$

has an austenite minima at $(e_2, e_3) = (0, 0)$, and $N_v = 3$ martensite minima at which $(e_2, e_3) = (\cos \phi, \sin \phi)$ for $\phi = 0, \frac{2\pi}{3}, \frac{4\pi}{3}$. Here $\vec{e}^2 \equiv e_2^2 + e_3^2$, and $\tau = (T - T_c)/(T_0 - T_c)$ is the scaled temperature; T_0 is the first-order Landau transition temperature and T_c is metastable austenite spinodal temperature.

The scaled Landau free energy \bar{F}_L for SO transition¹¹

$$\bar{F}_L(\vec{e}) = \sum_{\vec{r}} \tau \vec{e}^2 - (4 - C'_4/2) \vec{e}^4 + 4\vec{e}^6 - C'_4 e_2^2 e_3^2, \quad (2.3)$$

also has an austenite minima at $(e_2, e_3) = (0, 0)$, and $N_v = 4$ martensite minima at which $(e_2, e_3) = (\cos \phi, \sin \phi)$ for $\phi = \frac{\pi}{4}, \frac{3\pi}{4}, \frac{5\pi}{4}, \frac{7\pi}{4}$ with material dependent elastic constant C'_4 .

The scaled Landau free energy for TO transition¹¹ is

$$\bar{F}_L(\vec{e}) = \sum_{\vec{r}} (\tau - 1) \vec{e}^2 + \vec{e}^2 (\vec{e}^2 - 1)^2 + C_6 (\vec{e}^3 - (e_2^3 - 3e_2e_3^2))^2, \quad (2.4)$$

where C_6 is a material dependent parameter. The Landau polynomial has an austenite minima at $(e_2, e_3) = (0, 0)$, and $N_v = 6$ martensite minima at which $(e_2, e_3) = (\cos \phi, \sin \phi)$ for $\phi = 0, \frac{\pi}{6}, \frac{2\pi}{6}, \frac{3\pi}{6}, \frac{4\pi}{6}$ and $\frac{5\pi}{6}$.

The domain-wall cost Ginzburg term \bar{F}_G is,

$$\bar{F}_G(\vec{\nabla} \vec{e}) = \xi^2 \sum_{\vec{r}} (\vec{\nabla} \vec{e})^2 \quad (2.5)$$

The non-OP term is harmonic¹¹, with stiffness A_1 ,

$$\bar{F}_{non}(e_1) = \sum_{\vec{r}} \frac{A_1}{2} e_1^2 = \sum_{\vec{k}} \frac{A_1}{2} |e_1|^2 \quad (2.6)$$

and is minimized subject to St.Venant compatibility constraint for physical strains¹²,

$$\Delta^2 e_1 - (\Delta_x^2 - \Delta_y^2) e_2 - 2\Delta_x \Delta_y e_3 = 0; \quad (2.7a)$$

with gradient terms as difference operators $\vec{\nabla} \rightarrow \vec{\Delta}$ for sites \vec{r} on a computational grid. In Fourier space $k_\mu \rightarrow K_\mu(\vec{k}) \equiv 2 \sin(k_\mu/2)$ and so

$$O_1 e_1 + O_2 e_2 + O_3 e_3 = 0 \quad (2.7b)$$

where the coefficients for square lattice are $O_1 = -\frac{1}{\sqrt{2}} \vec{K}^2$, $O_2 = \frac{1}{\sqrt{2}} (K_x^2 - K_y^2)$, and $O_3 = 2K_x K_y$; for triangle lattice, $O_1 = -\vec{K}^2$, $O_2 = (K_x^2 - K_y^2)$, and $O_3 = 2K_x K_y$. Here, $\vec{K}^2 = (K_x^2 + K_y^2)$. Minimization of non-OP strain generates power-law anisotropic interactions between OP strains, by inserting a direct solution $e_1 = -(O_2 e_2 + O_3 e_3)/O_1$ for $\vec{k} \neq 0$ into (2.6),

$$F_{compat}(e_2, e_3) = \frac{A_1}{2} \sum_{\ell, \ell'=2,3; \vec{k}} e_\ell(\vec{k}) U_{\ell\ell'}(\vec{k}) e_{\ell'}^*(\vec{k}) \quad (2.8)$$

where $U_{22}(\vec{k}) = \nu(O_2/O_1)^2$, $U_{23}(\vec{k}) = \nu(O_2 O_3/O_1)^2$, $U_{33}(\vec{k}) = \nu(O_3/O_1)^2$ and $\nu = (1 - \delta_{\vec{k},0})$. Figure 2 shows the power-law potentials $U_{\ell\ell'}$ as relief plots in Fourier space and contours in coordinate space.

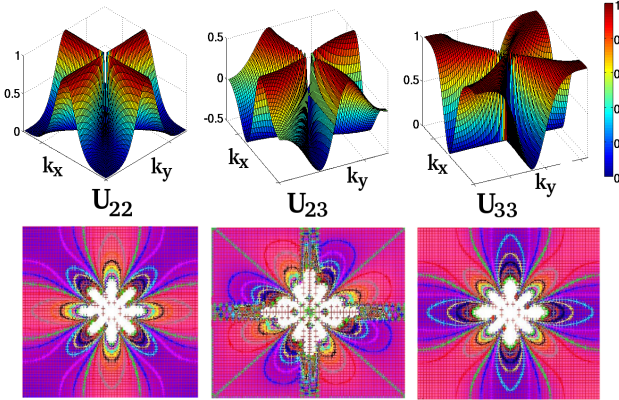


FIG. 2. *Power-law anisotropic potentials*: Relief plots of kernels $U_{22}(\vec{k})$, $U_{23}(\vec{k})$, and $U_{33}(\vec{k})$ in Fourier space (*top row*) and corresponding contours in coordinate space (*bottom row*).

The continuous-strain OP $\vec{e} = (e_2, e_3)$ is discretized¹¹ by choosing its values only at the $N_v + 1$ Landau minima,

$$\vec{e}(\vec{r}) = |e|(\cos \phi, \sin \phi) \rightarrow \bar{\varepsilon}(\tau) \vec{S}(\vec{r}). \quad (2.9)$$

The Landau term¹¹ becomes,

$$H_L(\vec{S}) = \bar{\varepsilon}^2 \sum_{\vec{r}} g_L(\tau) \vec{S}^2(\vec{r}) = \bar{\varepsilon}^2 \sum_{\vec{k}} g_L(\tau) |\vec{S}(\vec{k})|^2 \quad (2.10)$$

where $g_L = \tau - 1 + (\bar{\varepsilon} - 1)^2$, $\bar{\varepsilon}^2(\tau) = \frac{3}{4}\{1 + \sqrt{1 - 8\tau/9}\}$ for TCR, and $g_L = \tau - 1 + (\bar{\varepsilon}^2 - 1)^2$, $\bar{\varepsilon}^2(\tau) = \frac{2}{3}\{1 + \sqrt{1 - 3\tau/4}\}$ for SO and TO transitions.

The square gradient Ginzburg term becomes,

$$H_G(\vec{\nabla} \vec{S}) = \xi^2 \sum_{\vec{r}} \bar{\varepsilon}^2 (\vec{\nabla} \vec{S})^2 = \xi^2 \sum_{\vec{k}} K^2 \bar{\varepsilon}^2 |\vec{S}(\vec{k})|^2 \quad (2.11)$$

The discrete-strain pseudospin clock-zero model Hamiltonian is derived¹¹ by substituting (2.9) into the total free energy (2.1),

$$\beta H(\vec{S}) \equiv \beta F(\vec{e} \rightarrow \bar{\varepsilon} \vec{S}) \quad (2.12)$$

The Hamiltonian in coordinate space is

$$\beta H = \frac{D_0}{2} \left[\sum_{\vec{r}} \{g_L(\tau) \vec{S}^2(\vec{r}) + \xi^2 (\vec{\Delta} \vec{S})^2\} + \sum_{\vec{r}, \vec{r}'} \sum_{\ell, \ell'=2,3} \frac{A_1}{2} U_{\ell\ell'}(\vec{r} - \vec{r}') S_\ell(\vec{r}) S_{\ell'}(\vec{r}') \right], \quad (2.13a)$$

where $D_0 = 2E_0 \bar{\varepsilon}^2$. It is diagonal in Fourier space,

$$\beta H = \frac{1}{2} \sum_{\vec{k}} \sum_{\ell, \ell'=2,3} Q_{0, \ell\ell'}(\vec{k}) S_\ell(\vec{k}) S_{\ell'}^*(\vec{k}); \quad (2.13b)$$

$$Q_{0, \ell\ell'}(\vec{k}) \equiv D_0 [\{g_L(\tau) + \xi^2 \vec{K}^2\} \delta_{\ell, \ell'} + \frac{A_1}{2} U_{\ell\ell'}(\vec{k})], \quad (2.13c)$$

and is a clock-zero model Hamiltonian with single austenite $\vec{S} = (S_2, S_3) = (0, 0)$ and N_v martensite variants:

$$\vec{S} = (1, 0), \left(-\frac{1}{2}, \pm \frac{\sqrt{3}}{2}\right); \left(\pm \frac{1}{2}, \pm \frac{1}{2}\right); (\pm 1, 0), \left(\pm \frac{1}{2}, \pm \frac{\sqrt{3}}{2}\right) \quad (2.14)$$

for TCR ($N_v + 1 = 4$), SO ($N_v + 1 = 5$), and TO ($N_v + 1 = 7$) transitions respectively.

MC temperature-quench simulations are carried out systematically¹⁴ on a square lattice in 2D. At $t = 0$, we consider 2% of sites randomly with N_v strain-pseudospin martensite values in austenite. The seeds are quenched below the Landau transition $\tau \ll 1$ and held for $t \leq t_h$ MC sweeps (MCS). Metropolis algorithm is used for acceptance of energy changes, that are calculated through Fast Fourier transforms. In each MC sweep, we visit all $N = L \times L$ sites randomly, but only once. Simulation parameters are $L = 64, T_0 = 1; T_c/T_0 = 0.6, 0.7, 0.8, 0.9, \xi = 1; A_1 = 1, 4, 10; 2A_1/A_3 = 1; E_0 = 3, 4, 5, 6; t_h \leq 10,000$ sweeps, and conversion times are averaged over $N_{runs} = 100$ runs.

III. ATHERMAL AND ISOTHERMAL PARAMETER REGIMES

On quenching 2% of martensite seeds to a temperature $\tau(T) < \tau(T_0)$, we define¹⁴ martensite conversion fraction

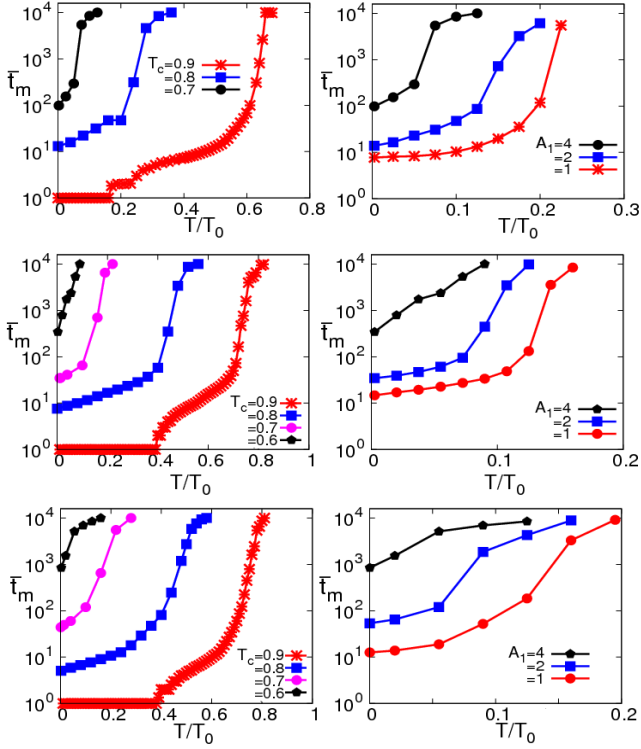


FIG. 3. *Crossover behaviour of athermal/isothermal martensite conversions: Left:* Conversion times \bar{t}_m vs T/T_0 showing crossover from athermal (fast) to intermediate (slow) for fixed $E_0 = 3$, $A_1 = 4$ and $T_c = 0.9, 0.8, 0.7$. *Right:* Conversions showing crossover from intermediate (slow) to athermal (fast) for fixed $E_0 = 3$, $T_c = 0.7$ and $A_1 = 4, 2, 1$. *Top row:* TCR, *middle row:* SO, and *bottom row:* TO transitions.

$n_m(t)$, which is equal to 0 in the pure austenite and 1 in the pure/twinned martensite,

$$n_m(t) = \frac{1}{N} \sum_{\vec{r}} \bar{S}^2(\vec{r}), \quad (3.1)$$

and specify conversion time $t = t_m$ when $n_m(t_m) = 0.5$.

From Figure 3, we can see isothermal slow conversions and athermal fast conversions with incubation-delay tails for different material parameters $A_1, T_c/T_0$ in TCR, SO, and TO transitions. Figure 3 also shows crossover from athermal to isothermal by fixing A_1 and changing T_c/T_0 , and vice versa. Hence, we find the martensite classification is a matter of material parameters: the same model Hamiltonian can show both athermal or isothermal behaviour, dependent on parameters. This is just as in the SR case¹⁴.

The athermal/isothermal/austenite regime diagrams are obtained in material parameters $T_c/T_0, A_1$ and shown in Figure 4, that clearly depicts athermal martensites are more common than isothermal². The simulations data matches well with the estimates¹⁴ of theoretical boundaries. Here, the criterion for athermal is $\bar{t}_m = 10$ MCS; isothermal/intermediate is $\bar{t}_m = 1000$ MCS; and austen-

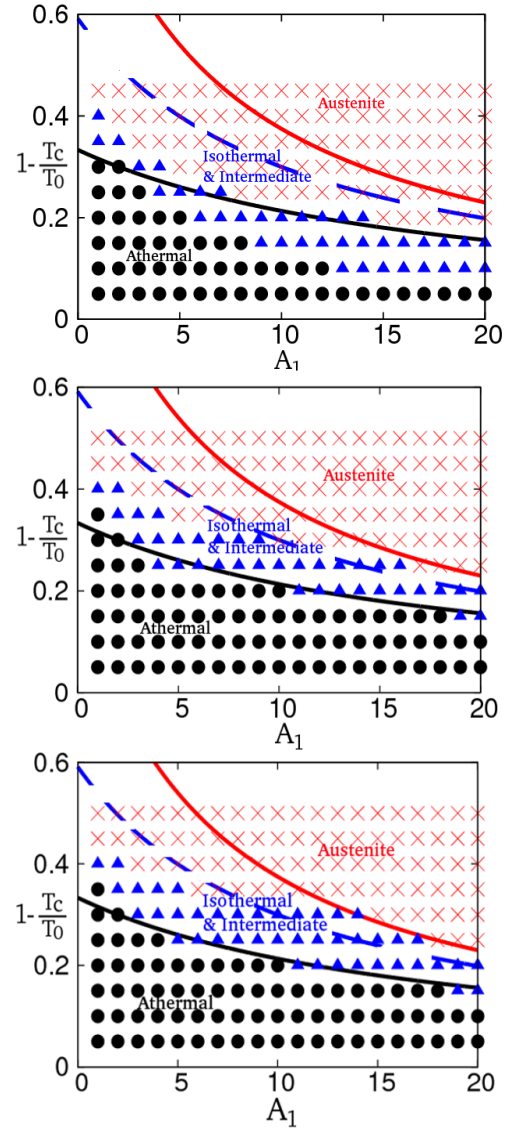


FIG. 4. *Athermal/isothermal martensite and austenite phase regimes:* Data of athermal, intermediate, and austenite behaviour in a plot of $1 - \frac{T_c}{T_0}$ versus A_1 , with $E_0 = 3$ for TCR (top), SO (middle) and TO (bottom) transitions. Estimates of the theoretical boundaries are shown as solid lines. See text.

ite, if there are no conversions even for holding time $t = t_h$. Again this is just as in the SR case¹⁴.

We will focus on the athermal regime. Figure 5 shows single-seed runs of $n_m(t)$ vs t after quenches to various $\Delta\tau \equiv \tau - \tau_4 < 0$, below the transition temperature $\tau_4 \equiv \tau(T_4)$. At low temperatures, $n_m(t)$ rises rapidly to unity, but as transition is approached, shows *incubation* behaviour. In the case of TCR transition, $n_m(t)$ rises to a smaller value, that incubates for longer times before it rises sharply to unity. In SO transition, $n_m(t)$ shows incubation followed by jerky steps before it rises to unity. In TO transition, $n_m(t)$ has longer incubations before it sharply rises to unity. The transition

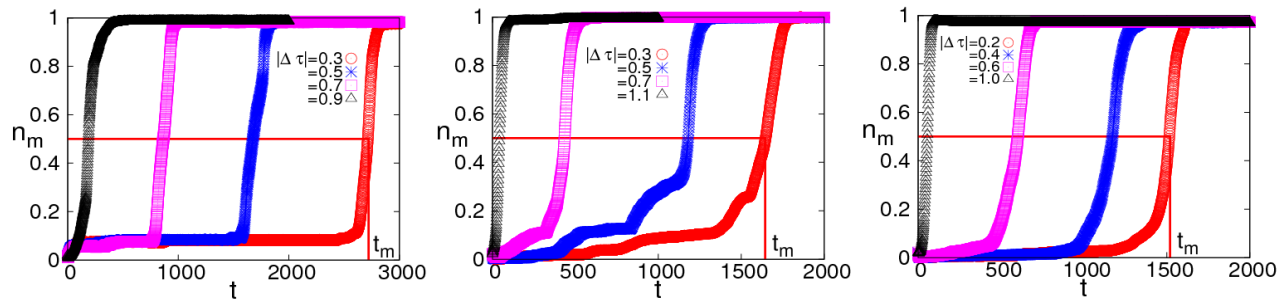


FIG. 5. *Conversion incubation times*: Martensite conversion fraction $n_m(t)$ versus time t , for stiffness $A_1 = 4$ and various $\Delta\tau \equiv \tau - \tau_4 < 0$, showing the 50% conversion definition of t_m for TCR (left), SO (middle) and TO (right) transitions. As athermal regime parameters have been chosen, flat incubation is seen for early times.

is 'fuzzy' and is operationally defined as where all 100 runs give austenite. Hence, we define¹⁴ mean conversion time $\bar{t}_m = 1 / \langle r_m \rangle$, where mean conversion rate $\langle r_m \rangle = \langle 1/t_m \rangle$ is obtained by an arithmetic average over $N_{runs} = 100$ seeds.

We henceforth focus on the athermal martensite parameter regime to study the conversion-delays kinetics.

IV. TEXTURAL ENERGIES PARAMETRIZED BY SURROGATE DROPLETS

The transition is known to depend both on temperature and the size of martensitic seeds, as in the Pati-Cohen model³. In early work, Pati and Cohen³ have measured and modeled the conversion times in Ni-Mn alloys and found that the isothermal slow conversions can change to athermal fast conversions, for fixed martensite fraction, but with larger (and hence fewer) initial martensite seeds. This can be understood through the parametrization of textural droplet energies as in SR transition¹⁴. At $t = 0$, the seeds of N_v variants are randomly sprinkled throughout the lattice. We find that the interaction tend to cancel leaving only self-interaction part $A_1[U]/2$ at each seed. So we have,

$$\beta H[\vec{S}(0)] \simeq \frac{D_0}{2} \sum_{\vec{r}} [g_L \vec{S}(\vec{r}, 0)^2 + \xi^2 \{\bar{\Delta} \vec{S}(\vec{r}, 0)\}^2 + \frac{A_1[U]}{2} \vec{S}(\vec{r}, 0)^2]. \quad (4.1)$$

Here, $[U] \simeq 0.5$, is the Brillouin-zone average of $U_{\ell\ell'}(\vec{k})$ of (2.8) in TCR, SO, and TO transitions. For an initial martensite fraction $n_m(0) = 0.02$, we have N_v variants square seeds of sides $R(0)$. The initial pseudospin seed energy is parametrized as $\beta H(\vec{S}(0)) = C_0[\alpha_L g_L R(0)^2 + \alpha_G \xi^2 4R(0) + \alpha_C (A_1[U]/2)R(0)^2]$ with $C_0 \equiv (n_m(0)ND_0/2)$. For different sides $R(0) = 1, 2, 3$, we fit the coefficients $\alpha_{L,G,C}$ term-by-term, finding again $\alpha_L = \alpha_G = \alpha_C = 1$, independent of seed size. Then

the initial energy has a droplet-like form $\beta H(R(0)) = C_0 2\xi^2 R_c [1 - (1 - R(0)/R_c)^2]$. Here we define a length $R_c(\tau)$ that is positive below a divergence temperature $\tau = \tau_L(A_1)$,

$$R_c(\tau) \equiv \frac{-2\xi^2}{g_L(\tau) + A_1[U]/2}. \quad (4.2)$$

As in the SR case, we define a scaled temperature variable $\eta(\tau)$ from the parametrization

$$\eta(\tau) = -R(0)/R_c(\tau) = \frac{g_L(\tau) + A_1[U]/2}{2\xi^2}, \quad (4.3)$$

that will be used later, for $R(0) = 1$.

At $t = 0$, the initial seeds have a geometric meaning, and hence the pseudospin Hamiltonian $H(\vec{S}(0))$ matches the droplet Hamiltonian $H(R(0))$, but for general t , these two terms no longer match term-by-term. However, as in SR case, we define $R(t)$ through $H[\vec{S}(t)]/H[\vec{S}(0)] = H[R(t)]/H[R(0)]$. The energy (ratio) for interacting *vector* pseudospins is parametrized, by the energy (ratio) of a surrogate system of independent droplets. The initially geometric $R(0)$ evolves to an interacting-texture energetic parameter $R(t)$, that can even go negative as the pseudospin energy goes negative. Thus

$$\begin{aligned} \rho(t) &\equiv \beta H(\vec{S}(t))/\beta H(\vec{S}(0)) \\ &= [1 - (\frac{R(t)}{R_c} - 1)^2]/[1 - (\frac{R(0)}{R_c} - 1)^2]. \end{aligned} \quad (4.4)$$

The $R(t)$ evolution is then once again

$$R(t)/R_c = 1 + \alpha \sqrt{1 - \rho(t)/\rho_c}, \quad (4.5)$$

where $\rho_c \equiv [1 - (\{R(0)/R_c\} - 1)^2]^{-1}$, and we take $\alpha = \text{sign}(\{R(0)/R_c\} - 1)$.

Figure 6 shows the evolutions of effective droplet energy in a plot of $R(t)/R_c(\tau)$ versus time. There are both rapid rises to final positive values and flat-incubations as already seen in the martensite conversion fraction n_m ,

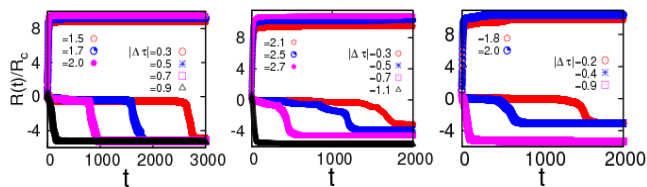


FIG. 6. *Trajectories* : Scaled energy parameter $R(t)/R_c$ versus time t , showing flows are determined by initial $R(0)/R_c(\tau)$ values. Note flat incubations of lower curves, of initial $1 > R(0)/R_c(\tau) > 0.5$, corresponding to $\tau_2 < \tau < \tau_4$ for TCR (left), SO (middle) and TO (right) transitions.

which goes negative at later times. The flat-incubations are due to the inefficient searches for the rare channels to lower energies. The initial $R(0)/R_c$ values determine the $R(t)$ flows.

As a consistency test of parametrization, Figure 7 shows $\rho(t)/\rho_c$ versus $R(t)/R_c$ indeed matches a parabola, for all t , and all A_1 , and many starting values $R(0)/R_c(\tau)$ in TCR, SO, and TO transitions. Flow directions of $R(t)$ are indicated by arrows starting at $R(0)/R_c$ for Regions 1,2,3,4, with asymptotic $R(t)$ giving negative final martensitic energies, or zero (going to austenite).

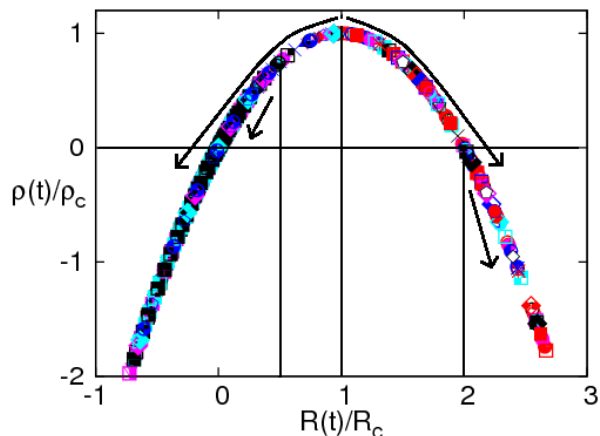


FIG. 7. *Parametrization and crossover temperatures* : Scaled pseudospin energy $\rho(t)/\rho_c$ versus $R(t)/R_c(\tau)$, showing flows fall on a parabola as a test of parametrization. For $R(0) = 1$ seeds, characteristic initial values $R(0)/R_c$ are $R_{c1}^{-1} = 2$, $R_{c2}^{-1} = 1$, $R_{c4}^{-1} \simeq 0.5$ as marked. These correspond to temperatures τ_1, τ_2, τ_4 . For initial $R(0)/R_c \lesssim 0.5$, flows are to $R = 0$ austenite.

i) *Region 1*: For initial $R(0)/R_c(\tau) > 2$, there are explosive conversions to martensite, this determines a temperature $\tau = \tau_1$ or $1/R_c(\tau_1) = 2$ or in scaled variable $\eta(\tau) = -2$ with initial unit seeds $R(0) = 1$.

ii) *Region 2*: For initial droplets $2 > R(0)/R_c(\tau) > 1$, the flows are again fast, this determines a temperature $\tau = \tau_2$ where $1/R_c(\tau_2) = 1$ or $\eta(\tau) = -1$.

iii) *Region 3*: For $0.5 \gtrsim R(0)/R_c(\tau)$ or $\eta(\tau) \gtrsim -0.5$,

the initial droplets are flowing only to $R = 0$ austenite. But, for larger A_1 , the droplets can still grow through searches up to $R(0)/R_c(\tau) \simeq 0$ or $\eta(\tau) \simeq 0$, that is well below the Landau transition temperature T_0 .

iv) *Region 4*: For $0.5 \lesssim R(0)/R_c(\tau) \lesssim 1$, the initial droplets immediately convert to a single variant droplet, that incubates for long times around $R(t) \simeq 0$ with zero energy $H \simeq 0$ (degenerate with austenite). This entropically critical droplet searches for conversion pathways, and grows through jerky steps and autocatalytic twinning. The incubations occur for unit seeds up to a temperature $\tau = \tau_4$ or $1/R_c(\tau_4) \simeq 0.5$ or in scaled variable $\eta(\tau) = -0.5$.

These critical values of the scaled variable $\eta(T, A_1)$ are used in the scaled plot of Fig. 8.

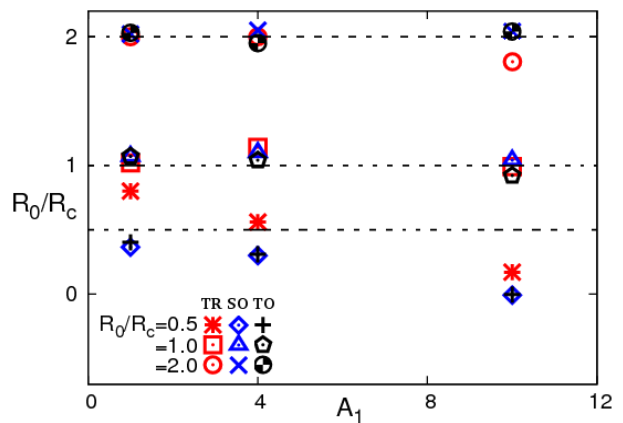


FIG. 8. *Textural crossover temperatures* : Phase diagram R_0/R_c vs A_1 . Theoretical boundaries (shown as dotted lines) in τ_1, τ_2, τ_4 are defined by $R_c(\tau_{1,2,4}) = R_{c1,c2,c4}$ of Fig 7 and symbols are data from simulations. See text.

V. ATHERMAL REGIME CONVERSIONS

In this Section, we find the conversion times and their distributions with a data collapse in terms of a scaled temperature-stiffness variable; and textural evolutions.

A. Conversion time and their distributions

The conversion times for different material parameters A_1, E_0 and for TCR, SO, and TO transitions fall on a single hyperbola in $\log \bar{t}_m$ versus $\Delta\tau \equiv \tau - \tau_4$, for a range of temperatures $\tau_4 < \tau < \tau_1$ as shown in main Fig 9. The same data is plotted in inset as $1/\ln(\bar{t}_m)$ versus $|\Delta\tau|/|\tau_1 - \tau_4|$, that shows linearity on $|\Delta\tau|$ goes to zero. The hyperbola and the linearity are showing the Vogel-Fulcher behaviour¹⁵. Specifically, $\bar{t}_m = t_0 \exp[b_0|\tau_1 - \tau_4|/|\tau - \tau_4|]$, with $t_0 = 1.6$, $b_0 = 1.7$, for these data. The insensitivity of conversion times \bar{t}_m

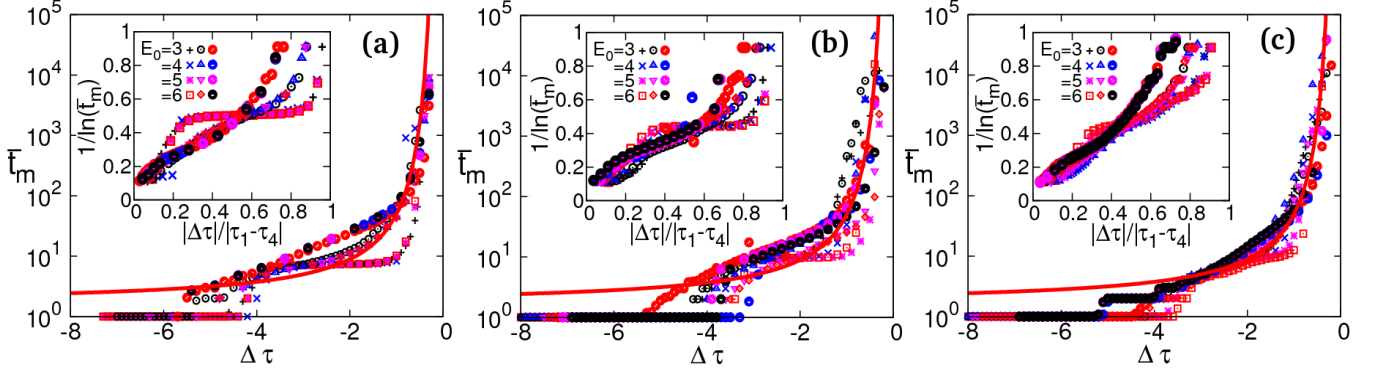


FIG. 9. *Singular divergence of conversion times*: Plot of $\ln \bar{t}_m$ vs $|\Delta\tau| \equiv |\tau - \tau_4|$, for (a) TCR, (b) SO and (c) TO transitions with $T_c/T_0 = 0.9$, $E_0 = 3, 4, 5, 6$ and $A_1 = 1, 4, 10$. Solid line is $\ln \bar{t}_m = \ln t_0 + b_0|\tau_1 - \tau_4|/|\Delta\tau|$, with $t_0 = 1.6$ and $b_0 = 1.7$.

to energy scales E_0 implies that the Vogel-Fulcher behaviour at τ_4 comes from divergence of entropy (rather than energy) barriers, $\bar{t}_m \sim e^{|\Delta S_{entr}|}$ in finding the rare channels¹⁶. The entropy barriers then vanish at τ_1 , with a drop in conversion times.

The main Figure 9 shows the temperature dependence of conversion times¹⁷ for TCR, SO, and TO transitions. As in the scalar-OP SR transition, there are explosive conversions below a temperature $\tau \simeq \tau_1$ (that is different for different transitions); and there are conversion delays for $\tau \gtrsim \tau_1$, that rise at $\tau \simeq \tau_2$, to diverge at a temperature $\tau \simeq \tau_4$. The success conversion fraction ϕ_m versus $\Delta\tau$ for various $A_1 = 1, 4, 10$ and $E_0 = 3, 4, 5, 6$ with fixed $T_c = 0.9$ for TCR, SO, and TO transitions is shown in Supplemental Material. The fraction ϕ_m is unity for $\tau \lesssim \tau_2$ and decreases for $\tau > \tau_2$, to become zero at $\tau \simeq \tau_4$. The insensitivity to different barrier energy scales E_0 is again a signature of entropy barriers¹⁶.

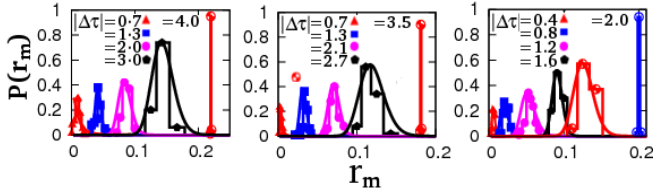


FIG. 10. *Log-normal distribution of conversion-rates*: Plot of $P(r_m)$ versus r_m for different $\Delta\tau$. Data are from Fig.9, with $A_1 = 4$, $E_0 = 3$ for TCR (left), SO (middle) and TO (right) transitions. Solid lines are the log-normal distributions.

Similar to the SR transition, we have calculated the arithmetic mean rate $\langle r_m \rangle \equiv 1/\langle t_m \rangle$ that determines $\bar{t}_m = 1/\langle r_m \rangle$, with $1/t_h < r_m < 1$ in TCR, SO, and TO transitions. The variance in the rates is $\sigma_r^2 = \langle (r_m - \langle r_m \rangle)^2 \rangle$. The probability densities $P(r_m)$ versus r_m for various $\Delta\tau$ are shown in the Figure 10, as histograms for different temperatures. For each histogram of N_{hist} data points, the Scott optimized bin size¹⁸ is used, of $dr_m = 3.5\sigma_r/[N_{hist}]^{1/3}$. The histograms

again narrow sharply, below τ_2 , as in the delta-function-like peak on the right. Solid lines are Log-normal curves for calculated $\langle r_m \rangle$ and σ_r^2 from the data. The Log-normal distribution is a signature of rare events¹⁹.

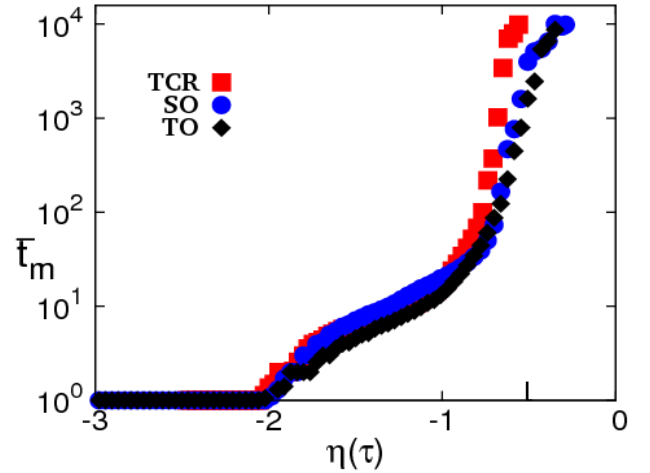


FIG. 11. *Temperature-Time-Transformation phase diagram*: Conversion times \bar{t}_m versus scaled variable $\eta(\tau)$ for TCR, SO, and TO transitions showing fast and delayed conversions for given parameters $A_1 = 4$, $E_0 = 3$, $T_c/T_0 = 0.9$.

Figure 11 shows TTT phase diagram in conversion times \bar{t}_m versus scaled variable $\eta(\tau) = -1/R_c(\tau)$ for fixed $A_1 = 4$, $E_0 = 3$ for TCR, SO, and TO transitions. The characteristic temperatures $\tau_{1,2,4}$ are defined in terms of scaled variable as $\tau = \tau_1$ or $\eta(\tau) = -2$ where $\bar{t}_m \simeq 1$ MCS; $\tau = \tau_2$ or $\eta(\tau) = -1$ where $\bar{t}_m \simeq 10$ MCS; and $\tau = \tau_4$ or $\eta(\tau) = -0.5$, where conversion times diverges.

VI. EVOLUTION OF TEXTURES

In the athermal parameter regime, after quenching into $\tau_4 > \tau > \tau_2$, we monitor evolution of OP strain \bar{S} tex-

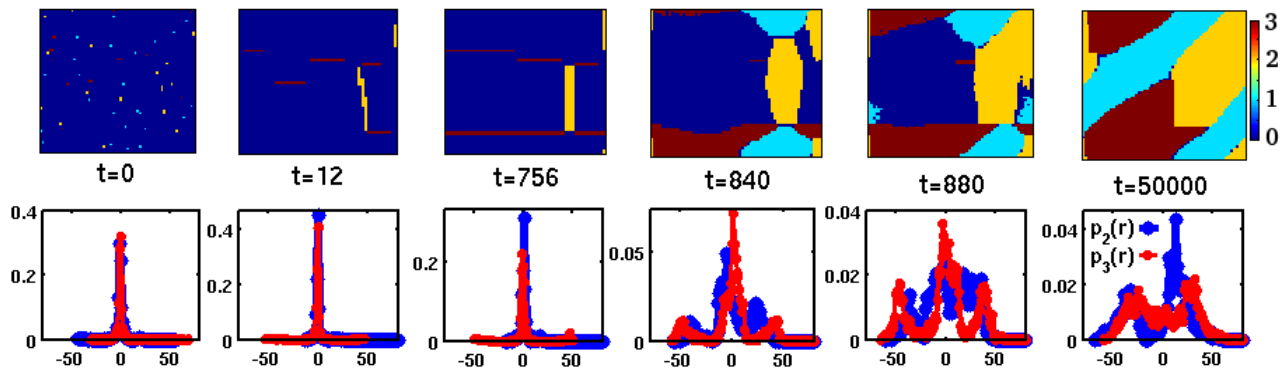


FIG. 12. *Evolution for the Triangle-centered rectangle (TCR) transition:* First row: Snapshots of OP strain $\vec{S} = (S_2, S_3)$ for different times t on quenching to $\tau = -2.7$. See movie of this evolution. The color bar is in terms of variant label V . See text. Second row: Evolving stress distributions of $p_2(\vec{r}), p_3(\vec{r})$. Parameters: $A_1 = 4, E_0 = 3$.

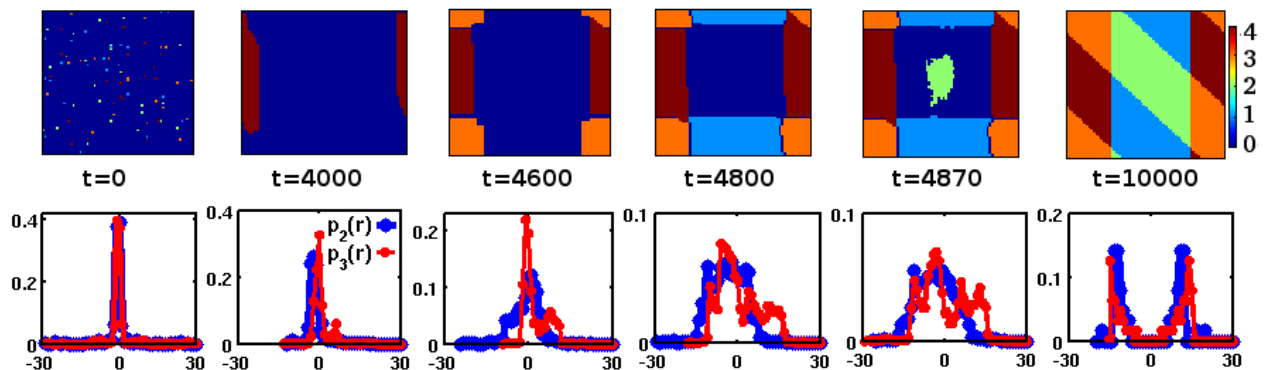


FIG. 13. *Evolution for the Square-oblique (SO) transition:* First row: Snapshots versus time t , of OP strain $\vec{S} = (S_2, S_3)$ on quenching to $\tau = -1.1$. The colour bar is in terms of variant label V . See movie. Second row: Evolving stress distributions $p_2(\vec{r}), p_3(\vec{r})$. Parameters: $A_1 = 4, E_0 = 3$.

tures, local internal stresses (See Appendix.) and stress distributions to understand the conversion-incubations at microstructure level. The color bar in Figs 12, 13, 14, 15 represents the OP strain \vec{S} in terms of variant label V . In all the three transitions, $V = 0$ represents austenite $\vec{S} = 0$ and $V = 1, 2, \dots, N_v$ corresponds to N_v martensite variants with pseudospin vector values given in (2.14), and pictured in Fig 1.

As shown in Figs. 12, 13, 14 (first row), after quenching the austenite with 2% martensite seeds into $\tau_4 > \tau > \tau_2$, the seeds quickly form domain-wall 'vapour' of droplets of single variant(s), reminding Ostwald ripening. The droplets searches for the rare pathway channels to expand in the easy directions of the anisotropic potential. The expanded droplet then generates the other variant by autocatalytic twinning as in Bales and Gooding^{7,11} to form 'liquid' of domain-walls, which orient to form domain-wall 'crystal' at a later time. The jerkiness during conversion incubation is reflected in wavenumber k_m (not shown) as steps with finite values^{14,20} and also in (excess) thermodynamic quantities^{14,20}, internal energy

ΔU and entropy $-T\Delta S$ (not shown).

In the second row of Figs. 12, 13, 14, the local stress distributions $p_2(\vec{r}), p_3(\vec{r})$ are shown. At $t = 0$, the stress distributions are sharply peaked around zero with large values, which generate wings on both sides of the peak during autocatalytic twinning. In the final oriented state, only the wings remain, that correspond to the trapped stress values along the domain-walls (except in TO case, where $p_3(\vec{r})$ is sharply peaked around zero).

The final 'equilibrium' microstructures in the TTT phase diagram for TCR, SO, and TO transitions are shown in Figure 15 and are in good agreement with continuous variable simulations⁵⁻⁷ and experiments¹⁰.

With random initial seeds, there is a vibrating martensite phase, that has bulk austenite in TCR, SO, and TO transitions as in Fig.15 (a), that could be equivalent of the chequerboard SR case tweed pattern¹⁴ (and becomes less probable closer to $\tau \simeq \tau_4$).

With 2% of martensite seeds, and for $\tau > \tau_4$ or $\eta(\tau) \gtrsim -0.5$, there is only uniform austenite. For $\tau_2 \lesssim \tau \lesssim \tau_4$ or $-1 \lesssim \eta \lesssim -0.5$, there are again austenite droplets but now appear as lines, in domain wall crystal (DWC)

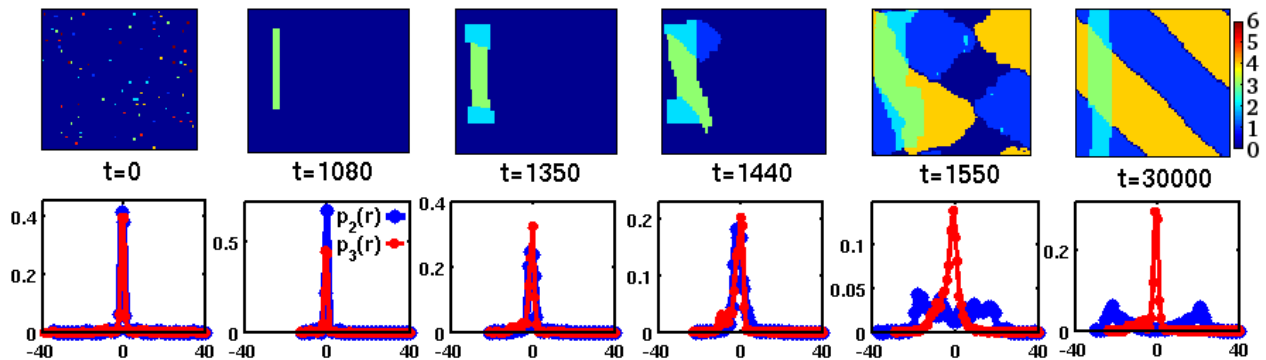


FIG. 14. *Evolution for the Triangle-oblique (TO) transition: First row: Snapshots of the OP strain $\vec{S} = (S_2, S_3)$ evolution in terms of V on quenching to $\tau = -1.1$. See movie. Second row: Stress distributions $p_2(\vec{r}), p_3(\vec{r})$. Parameters: $A_1 = 4, E_0 = 3$.*

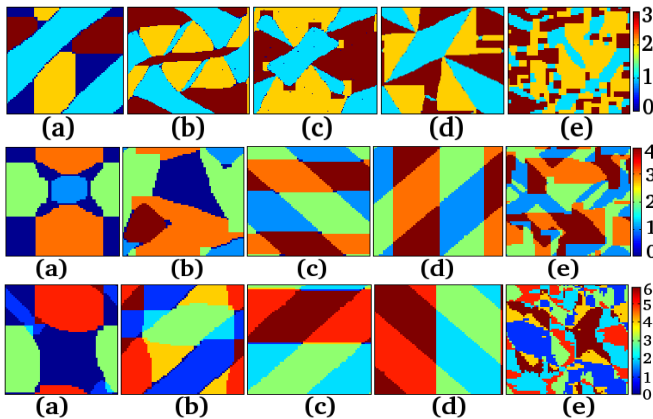


FIG. 15. *Final 'equilibrium' microstructures: The long time textures are shown, for transitions TCR, SO, and TO are in the first, second and third rows, respectively. (a) precursor vibrating phase (bulk-austenite) for $\tau \simeq \tau_4$; (b) and (c) fan-like and Z-shaped twins (austenite appears as point or line densities) for $\tau_2 \gtrsim \tau \gtrsim \tau_4$; (d) star-like or martensite twins (no bound austenite) for $\tau_1 \gtrsim \tau \gtrsim \tau_2$; (e) glass for $\tau \ll \tau_1$. The austenite is represented as zero in color bar. Parameters are typically $A_1 = 4, T_c = 0.9, \xi^2 = 1$ and $E_0 = 3$.*

in SO, TO cases, and Z-like states¹⁰ in TCR case as in Fig.15 (b). For $\tau_1 \lesssim \tau < \tau_2$ or $-2 \lesssim \eta(\tau) < -1$, austenite droplets can appear as points at corners, in DWC (that have topological charges) in SO, TO cases; and also fan-like oriented states¹⁰ in TCR case as shown in Fig.15 (c). At low temperatures for $\tau \ll \tau_1$ or $\eta(\tau) \ll -2$, the DWC or oriented twins can have vortex-like (or topological defects or charges) behaviour at multi-variant junctions in SO¹⁰, TO cases, and partially oriented star-like states¹⁰ in TCR case, can compete with a frozen domain wall liquid or 'glass' as shown in Fig.15 (d), (e), and has no bound austenite. Hence, τ_1 is austenite (local) spinodal temperature. The microstructure (d) as shown in Fig.15 (first row) for TCR transition is not fully relaxed even after $t_h = 10^6$ MCS and could possibly take longer

and longer times, to orient fully to a nested star as seen in continuous variable simulations and experiments^{5-7,10}.

VII. CONVERSIONS WITHOUT THE COMPATIBILITY INTERACTION

We now turn-off the compatibility term ($A_1 = 0$) in the Hamiltonians for TCR, SO and TO transitions to understand the role of the power-law anisotropic potentials in the domain-wall conversion kinetics.

Figure 16 showing the martensite fraction $n_m(t)$ versus time t for different temperatures $|\Delta\tau| = |\tau - \tau_4|$, where τ_4 is austenite transition temperature; and conversion times \bar{t}_m versus temperature $\Delta\tau$ for different energy scales E_0 for TCR, SO, and TO transitions with elastic stiffness constant $A_1 = 0$. Here, n_m has no flat regions or incubation as was seen for $A_1 = 4$ in Fig.5. The final microstructure in $A_1 = 0$ case is a slab-like martensite unlike oriented microstructures in $A_1 = 4$ as in Fig.15.

Conversion times show a rise at τ_1 , that almost remain constant till τ_2 and then increase linearly to τ_4 , above which there are no conversions found. There are no Vogel-Fulcher rises in conversion times as in $A_1 = 4$ (Fig.9), but there is a small E_0 dependence, which could be now from energy barriers rather than entropy barriers.

With the parametrization scale of (4.2) now given by $R_c(A_1 = 0) = 2\xi^2/|g_L|$, the estimated transition temperatures are $\tau_1 = -5.5, -4.0, -4.0$; $\tau_2 = -2.0, -1.4, -1.4$; $\tau_4 = -0.4, -0.2, -0.2$ are in good agreement with the simulation values of $\tau_1 = -5.5, -4.0, -4.0$; $\tau_2 = -2.0, -1.4, -1.4$; $\tau_4 \simeq -0.8, -0.1, -0.1$ for TCR, SO, and TO transitions respectively.

Therefore, microstructures and conversion times in TCR, SO, and TO transitions with $A_1 = 0$ are clearly different from the non-zero A_1 case. Thus, the power-law anisotropic potentials in ferroelastic transitions are important in understanding orientations and kinetics of domain-walls.

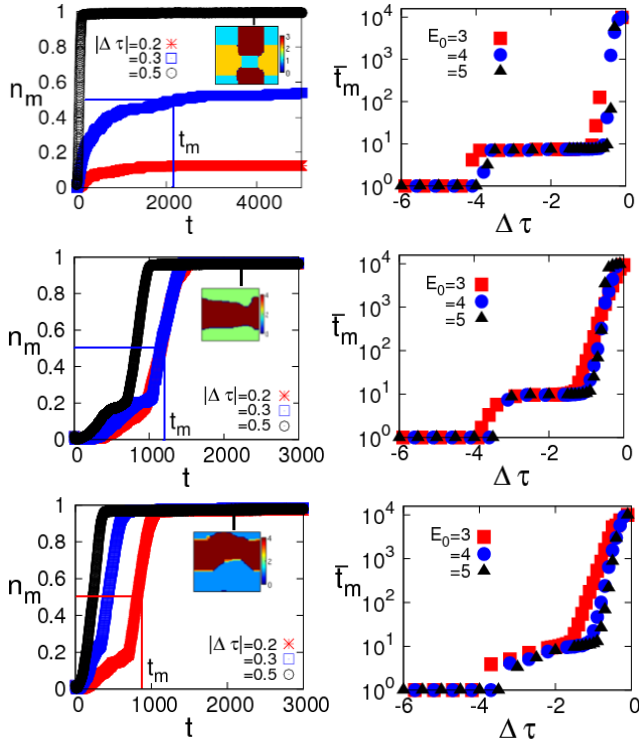


FIG. 16. *Microstructures and conversion times with $A_1 = 0$* : The left column shows martensite fraction $n_m(t)$ versus t for $|\Delta\tau| = 0.2, 0.3, 0.5$ and $E_0 = 3$, with the conversion time t_m is marked for TCR (*top row*), SO (*middle row*), and TO (*bottom row*). The right column shows the conversion times t_m versus $\Delta\tau$ for $E_0 = 3, 4, 5$. Compare to Fig 5 and Fig. 9, respectively.

VIII. SUMMARY AND FURTHER WORK

Systematic temperature-quench MC simulations without extrinsic disorder are carried on the strain pseudospin clock-zero model Hamiltonians, with vector-order parameter ($N_{OP} = 2$) and $N_v + 1 (= 4, 5, 7)$ strain-pseudospins, that correspond to triangle-to-centred rectangle, square-to-oblique, and triangle-to-oblique transitions to get insights into conversion-incubation kinetics. The results are similar to the SR case¹⁴, that are just seen to be generic. The simulation results are as follows:

(1) The microstructures of discrete-strain pseudospins in the Temperature-Time-Transformation phase diagram are in good agreement with continuous-variable simulations and experiment.

(2) On quenching, for different material parameters $T_c/T_0, \xi^2, A_1, E_0$, martensite fraction $n_m(t)$ can have slow isothermal and fast athermal conversions. The conversion times t_m can transform from rapid athermal to slow isothermal or vice versa on changing the material parameters; and athermal/isothermal/austenite regime diagrams are obtained in material parameters.

(3) Focusing on the athermal parameter regime, we

find rapid conversions below a spinodal like temperature and incubation delay above it, as in the experiment. The conversion-delay times have Vogel-Fulcher divergences, which are insensitive to Hamiltonian energy scales E_0 and conversion rates have Log-normal distributions, as in scalar-OP SR transition, from entropy barriers.

(4) The Temperature-Time-Transformation diagram in the athermal parameter regime has crossover temperatures and are understood through parametrization of domain wall textures by surrogate droplet energies.

(5) During conversion incubation (t_m), evolutions of microstructures, stress distributions and domain-wall thermodynamics are monitored. The initial martensite seeds in the austenite at $t = 0$ disappear to form a domain-wall vapour of single variant droplet(s), that incubates before generating N_v variants, one after the other, by autocatalytic twinning to convert to domain-wall liquid. The wandering domain-walls then orient later to a domain-wall crystal. During incubation, stress distributions remain sharply peaked, and there are finite steps in (excess) internal energy, (excess) entropy.

(6) On switching off the power-law anisotropic potentials, we find no incubations in conversions, no Vogel-Fulcher divergences and the microstructure is multi-slab martensite.

Systematic experiments on athermal martensites can look for martensite formation and growth during conversion incubation and their divergences as well as distributions close to the transition.

Monte Carlo simulations presented in this paper are on 2D strain-pseudospin models for ferroelastic transitions with vector-OP. We also find similar conversion incubation-delays in 3D strain-pseudospin models for tetragonal-to-orthorhombic ($N_v = 2, N_{OP} = 1$), cubic-to-tetragonal ($N_v = 3, N_{OP} = 2$), cubic-to-orthorhombic ($N_v = 6, N_{OP} = 2$), and cubic-to-trigonal ($N_v = 4, N_{OP} = 3$) ferroelastic transitions²¹.

Acknowledgements: It is a pleasure to thank S.R. Shenoy, T. Lookman and K.P.N. Murthy for very helpful discussions, and S.R. Shenoy for help with the manuscript. The University Grants Commission, India is thanked for Dr. D.S. Kothari Postdoctoral Fellowship.

APPENDIX: INTERNAL STRESSES

The local internal stresses, $p_2(r) = \partial\bar{F}/\partial e_2(\vec{r})$, and $p_3(r) = \partial\bar{F}/\partial e_3(\vec{r})$ for TCR transition are obtained as,

$$p_2(r) = \epsilon[4\epsilon^3 S_2^3 - 6\epsilon S_2^2 + 2S_2(2\epsilon^2 S_3^2 + \tau) + 6\epsilon S_2^3 + 2\xi^2 \Delta^2 S_2 + A_1(U_{22}S_2 + U_{33}S_3)], \quad (A.1a)$$

$$p_3(r) = \epsilon[4\epsilon^2 S_3^3 + 2S_3(2\epsilon^2 S_2^2 + 6\epsilon S_2 + \tau) + 2\xi^2 \Delta^2 S_3 + A_1(U_{23}S_2 + U_{33}S_3)]. \quad (A.1b)$$

The local internal stresses for SO transition are,

$$p_2(r) = \epsilon[2S_2(3S_2^4 - 4S_2^2 + \tau) + 2\xi^2\Delta^2S_2$$

$$+A_1(U_{22}S_2 + U_{33}S_3)], \quad (A.2a)$$

$$p_3(r) = \epsilon[2S_2(3S_3^4 - 4S_3^2 + \tau) + 2\xi^2\Delta^2S_3$$

$$+A_1(U_{23}S_2 + U_{33}S_3)]. \quad (A.2b)$$

The local internal stresses for TO transition are,

$$p_2(r) = \epsilon[2S_2(3S_2^4 - 4S_2^2 + \tau) + 2\xi^2\Delta^2S_2$$

$$+A_1(U_{22}S_2 + U_{33}S_3)], \quad (A.3a)$$

$$p_3(r) = \epsilon[2S_2(3S_3^4 - 4S_3^2 + \tau) + 2\xi^2\Delta^2S_3$$

$$+A_1(U_{23}S_2 + U_{33}S_3)]. \quad (A.3b)$$

-
- ¹ K. Bhattacharya, *Microstructure of Martensite*, Oxford University Press, Oxford (2003);
- ² *Physical properties of martensite and bainite*: Proceedings of the joint conference organized by the British Iron and Steel Research Association and the Iron and Steel Institute, Special report **93**, London (1965).
- ³ A.R. Entwisle, *Metallurgical transactions* **2**, 2395 (1971); J.R.C. Guimaraes and P.R. Rios, *J. Mater. Sci.* **43**, 5206 (2008); G.V. Kurdjumov and O.P. Maximova, *Doklad. Akad. Nauk SSSR* **61**, 83 (1948); **73**, 95 (1950); S.R. Pati, M. Cohen, *Acta Metallurgica* **17**, 189 (1969).
- ⁴ T. Kakeshita, T. Fukuda and T. Saburi, *Scripta Mat.* **34**, 1 (1996); L. Mueller, U. Klemradt and T.R. Finlayson, *Mat. Sci. and Eng. A* **438**, 122 (2006); L. Mueller, M. Waldorf, C. Gutt, G. Gruebel, A. Madsen, T.R. Finlayson, and U. Klemradt, *Phys. Rev. Lett.* **107**, 105701 (2011); T. Kakeshita, J-M. Nam and T. Fukuda, *Sci. Techn. Adv. Mater.* **12**, 015004 (2011).
- ⁵ A.E. Jacobs, S.H. Curnoe and R.C. Desai, *Phys. Rev. B* **68**, 224104 (2003); S.H. Curnoe and A.E. Jacobs, *Phys. Rev. B* **63**, 094110 (2001); **64**, 064101 (2001).
- ⁶ Y.H. Wen, Y.Z. Wang and L.Q. Chen, *Philos. Mag. A* **80**, 1967 (2000); Y. Wang and A.G. Khachaturyan, *Mater. Sc. and Eng. A* **438**, 55 (2006).
- ⁷ G.S. Bales and R.J. Gooding, *Phys. Rev. Lett.* **67**, 3412 (1991); T. Lookman, S.R. Shenoy, K.Ø. Rasmussen, A. Saxena and A.R. Bishop, *Phys. Rev. B* **67**, 024114 (2003).
- ⁸ S. Kartha, T. Kastàn, J.A. Krumhansl, and J.P. Sethna, *Phys. Rev. Lett.* **67**, 3630 (1991); M. Baus and R. Lovett, *Phys. Rev. Lett.* **65**, 1781 (1990); *Phys. Rev. A* **44**, 1211 (1991).
- ⁹ M Rao and S. Sengupta, *Phys. Rev. Lett.* **91**, 045502 (2003); *Current Science* **77**, 382 (1999).
- ¹⁰ C. Manolikas and S. Amelinckx, *Phys. Stat. Sol. A* **60**, 607 (1980); *Phys. Stat. Sol. A* **61**,179 (1980); M. Ramudu, A. Satish Kumar, V. Seshubai, K. Muraleedharan, K.S. Prasad, and T. Rajasekharan, *Scr. Mater.* **63**, 1073 (2010).
- ¹¹ S.R. Shenoy, T. Lookman and A. Saxena, *Phys. Rev. B* **82**, 144103 (2010); S.R. Shenoy and T. Lookman, *Phys. Rev. B* **78**, 144103 (2008).
- ¹² R. Barsch, B. Horovitz, and J.A. Krumhansl, *Phys. Rev. Lett.* **59**, 1251 (1987); B. Horovitz, G.R. Barsch, and J.A. Krumhansl, *Phys. Rev. B* **43**, 1021 (1991);
- ¹³ R. Vasseur, T. Lookman and S. R. Shenoy, *Phys. Rev. B* **82**, 094118 (2010).
- ¹⁴ N. Shankaraiah, K.P.N. Murthy, T. Lookman and S.R. Shenoy, *Europhys. Lett.* **92**, 36002 (2010), *Phys. Rev. B* **84**, 064119 (2011); *J. Alloys Compd.* **577**, S66 (2013); *Phys. Rev. B* **91**, 214108 (2015).
- ¹⁵ K. Binder and W. Kob, *Glassy materials and disordered solids*, World Scientific, Singapore (2005).
- ¹⁶ F. Ritort, *Phys. Rev. Lett.* **75**, 1190 (1995); M. Mansfield, *Phys. Rev. E* **66**, 016101 (2002).
- ¹⁷ Figure 9 shows the t_h -independent data and also t_h -dependent conversion times, that are extracted from 'finite size scaling' in $1/t_h \rightarrow 0^{14}$. The t_h -independent linear portions in $1/\log(\bar{t}_m)$ versus τ are extrapolated to intersect the τ -axis, and a temperature τ_4 is defined, that almost matches with the operationally defined τ_4 in Figure 9.
- ¹⁸ D.W. Scott, *Biometrika* **66**, 605 (1979).
- ¹⁹ A. Shah, S. Chakravarty and J.K. Bhattacharjee, *Pramana* **71**, 413 (2008); A.N. Kolmogorov, *Dokl. Akad. Nauk SSSR* **30**, 301 (1941).
- ²⁰ N. Shankaraiah, *PhD Thesis*, University of Hyderabad, India (2012).
- ²¹ N. Shankaraiah, K.P.N. Murthy, T. Lookman, and S.R. Shenoy (unpublished).